# Structure signatures in proton scattering from $^{9,11}$Li

R. Crespo,[*] J. A. Tostevin, and I. J. Thompson

*Department of Physics, University of Surrey, Guildford, Surrey, GU2 5XH, United Kingdom*

(Received 11 December 1995)

The optical potential and observables for proton-$^{9,11}$Li elastic scattering are calculated microscopically using the single scattering approximation to the Kerman-McManus-Thaler multiple scattering expansion. The importance of the central and spin-orbit terms of the optical potential, and of the core and halo nucleon contributions, is clarified in terms of the momentum space behaviors of the nucleon-nucleon amplitudes and relevant density distributions. Calculations for the $^9$Li and $^{11}$Li systems at 60 and 62 MeV/nucleon, respectively, are compared with the available experimental data and with calculations and data for the proton-$^8$He system at similar energy. Three-body models of $^{11}$Li are used. The effects of the halo distribution in $^{11}$Li are clearly manifest in the elastic cross section but there are small differences between observables for structure models with realistic two-neutron asymptotic behaviors. Calculations suggest that the $^9$Li core structure is not realistically described by simple models. [S0556-2813(96)05009-1]

PACS number(s): 24.10.Ht, 21.10.Gv, 25.40.Cm, 27.20.+n

## I. INTRODUCTION

Experiments with radioactive nuclei from fragmentation reactions [1] have stimulated many structure studies of light nuclei near the neutron drip line. Radii of matter densities are now routinely deduced from cross section measurements [2–4] and show that some nuclei, close to the neutron drip line, exhibit a halo of diffuse neutron matter extending far beyond the protons and large matter radii in comparison with their stable isotopes [5], a direct consequence of low one- or two-neutron separation energies. One- and two-neutron halos have now been observed in several light neutron rich nuclei, such as $^{11}$Be and $^{11}$Li. The $n$ separation energy is 0.5 MeV in the case of $^{11}$Be and the $2n$ separation energy is 0.3 MeV for $^{11}$Li.

The formation of well-developed halos means that neutron rich nuclei represent qualitatively different many-nucleon systems. Conventional mean field approaches fail to reproduce the matter radii of halo nuclei without adjustment of the separation energy of the last neutron to measured values [6]. It is necessary to go beyond the mean field approximation and include additional correlations to describe these systems. $^{11}$Li is usefully treated as a $^9$Li$+n+n$ system, having no bound states in any of its binary subsystems. Three-body methods have thus been applied extensively to this system [7–9].

The interaction of nucleons with halo nuclei, and their elastic scattering, is a basic reaction mechanism which might permit an assessment of these halo structures. In the present work we calculate these interactions microscopically and the resulting scattering, taking structures calculated from three-body models. Our principal aim is not to fit the experimental data, but to study the effects on elastic scattering observables of different microscopic descriptions of the structure of the halo neutrons in $^{11}$Li when assuming simple models for the structure of the $^9$Li core, such as were successful for $^8$He

scattering [10]. For instance, some evidence has been accumulated [11] which points to the existence of a near-threshold $s$-wave virtual state in the $n + {}^9$Li ($^{10}$Li) system. If present, structure calculations show that this virtual state has a profound effect on the nature of the structure of the $^{11}$Li halo [12]. We assess the implications of these halo structures, and the assumed structure of the $^9$Li core, for observables in the elastic scattering of protons from $^9$Li and $^{11}$Li.

Measurements of the elastic scattering of protons from the lithium isotopes $^{9,11}$Li at about 60 MeV/nucleon [13] and from $^8$He at 72 MeV/nucleon [14] have been published. Phenomenological, Born approximation, and a variety of Glauber and forward scattering approximation models have been applied to these data [13,15–17]. All of the nonphenomenological analyses of the ion-nucleon interaction assume simplified or parametrized effective nucleon-nucleon ($NN$) interactions or transition amplitudes. A central zero-range effective $NN$ force is usually assumed. Traditional surface derivative spin-orbit potential terms have been used in phenomenological analyses [13,17] of the data for the Li isotopes. While such radial forms are justifiable for heavy nuclei with well-defined surfaces and small diffuseness parameters, their use for light nuclei, particularly those with a diffuse long range valence nucleon distribution, is suspect. This spin dependence should be calculated microscopically. In the multiple scattering approach used here, the central and spin-dependent terms of the nucleon-nucleus interaction are derived explicitly from those of a realistic $NN$ interaction, consistent with the assumed projectile density. It was already shown in [10], for $p$-$^8$He scattering, that elastic scattering observables show considerable sensitivity to both the spin-orbit component and to the finite range of the $NN$ interaction, in that case the Paris interaction, and that these are essential ingredients in quantitative studies.

In the present work, as in [10], we use the Kerman-McManus-Thaler (KMT) [18] multiple scattering treatment of the optical potential. Careful treatments of both the first and second order terms of the multiple scattering series have been carried out in recent years [19–22]. The single scattering approximation to the multiple scattering series has been

---

[*]Present and permanent address: Departamento de Física, Instituto Superior Técnico, Lisboa, Portugal.

applied with success for the description of elastic nucleon scattering data from a wide range of targets at 65 MeV [23] and for $p$-$^8$He scattering at 72 MeV [10]. As the multiple scattering approach expands the nucleon-ion optical potential in terms of a realistic free $NN$ transition amplitude and target wave function, the method allows first principles calculations of the optical potential based upon structure calculations and the free $NN$ interaction as inputs.

Unlike $N \approx Z$ nuclei, halo nuclei present two distinct regions of nuclear matter density to the scattered proton. The ground state density is the sum of contributions due to the core ($^9$Li in the $^{11}$Li case) and from the valence or halo nucleons. The nucleons in these two regions have different spin-isospin compositions and momentum distributions, and are thus probed by different terms of the $NN$ amplitude, and at different momentum transfers. It is considered extremely important to clarify this basic interplay between the range of the nuclear densities and the different terms of the $NN$ interaction, and to understand the extent to which microscopic calculations based on the free $NN$ amplitude are able to describe the available data prior to any complication of the physical description through the use of effective interactions. Such interactions, deduced from isospin symmetric systems, are largely untested quantitatively for the drip line systems of interest here.

We apply the single scattering KMT optical potential to the $^9$Li and $^{11}$Li systems. We consider two models for the core ($^9$Li) structure. The sensitivity of the $p$-$^9$Li elastic scattering observables to these models is assessed as are the effects of different structure models for the halo density on the $p$-$^{11}$Li elastic scattering observables. Calculations are presented for $p$-$^{9,11}$Li scattering at 60 and 62 MeV/nucleon, respectively, where cross section data are available. We compare these results with calculations and data for the proton-$^8$He system at similar energy. We clarify the roles of the central and spin-orbit parts of the optical potential arising from the core and halo nucleons by reference to the momentum space behaviors of the on-shell $NN$ amplitudes and the target density distributions. The presented results are expected to hold quite generally.

## II. MICROSCOPIC OPTICAL POTENTIAL

The first order term of the KMT optical potential for nucleon scattering from a target of mass $A$ is given by the expression [18,20]

$$U = \frac{A-1}{A} \sum_{n=1}^{A} \langle \Phi_0 | t_{0n}^f(\omega) | \Phi_0 \rangle. \tag{1}$$

Here $\Phi_0$ is the target nucleus wave function and $t_{0n}^f(\omega)$ is the $NN$ transition operator describing the free scattering of the incident (0) and struck ($n$) target nucleon with an energy parameter $\omega$. This transition amplitude satisfies the integral equation

$$t_{0n}^f(\omega) = v_{0n} + v_{0n} g(\omega) t_{0n}^f(\omega), \tag{2}$$

where $v_{0n}$ is the free space $NN$ interaction. The intermediate states propagator $g(\omega)$ is therefore

$$g(\omega) = \frac{1}{\omega^+ - K_{0n}}, \tag{3}$$

where $K_{0n}$ is the kinetic energy operator for the relative motion of the active $NN$ pair. Medium effects arising from distortions due to the struck nucleon binding potential have been neglected in the propagator [21]. The energy parameter is $\omega = E_0 - \hbar^2 \hat{\mathcal{P}}^2/4m$, where $\hat{\mathcal{P}}$ is the momentum operator for the motion of the center of mass (c.m.) of the interacting $NN$ pair [21], and $m$ is the nucleon mass. $E_0$ is the incident nucleon energy in the nucleon-target ($NA$) c.m. frame; thus, $E_0 = \hbar^2 k_0^2/2\mu_{NA}$, with $\mu_{NA}$ the nucleon-target reduced mass.

The second order term of the multiple scattering expansion, which takes into account Pauli blocking medium effects, has been investigated elsewhere in considerable detail [21]. Pauli blocking corrections are not considered explicitly here.

The matrix elements of the optical potential are developed in momentum space as

$$\langle \vec{k}' | U | \vec{k} \rangle = \frac{A-1}{A} \sum_{n=1}^{A} \langle \vec{k}' \Phi_0 | t_{0n}^f(\omega) | \vec{k} \Phi_0 \rangle. \tag{4}$$

Introducing the variable $\vec{Q} = (\vec{k} + \vec{k}')/2$, the mean value of the scattered nucleon momenta, then, within the optimal factorization limit [20],

$$\langle \vec{k}' | U | \vec{k} \rangle = \frac{A-1}{A} \sum_{n=1}^{A} \langle \Phi_0 | -\vec{q}/2 \rangle$$
$$\times \left\langle \frac{1}{2}\left( \vec{k}' + \frac{\vec{q}}{2} \right) \middle| t_{0n}^f(\omega) \middle| \frac{1}{2}\left( \vec{k} - \frac{\vec{q}}{2} \right) \right\rangle \langle \vec{q}/2 | \Phi_0 \rangle, \tag{5}$$

where $\vec{q} = \vec{k}' - \vec{k}$ is the momentum transfer and the energy parameter $\omega$ is now

$$\omega = E_0 - \frac{\hbar^2}{4m} Q^2. \tag{6}$$

In this momentum space form, Eq. (5), a $NN$ transition amplitude from realistic $NN$ interaction models can be included. With the convention that plane waves are normalized such that

$$\langle \vec{r} | \vec{k} \rangle = (2\pi)^{-3/2} \exp(i\vec{k} \cdot \vec{r}),$$

the antisymmetrized transition amplitude and $NN$ scattering amplitude $M$ are related according to

$$\langle \vec{\kappa}' | t_{0n}^f(\omega) | \vec{\kappa} \rangle = -\frac{\hbar^2}{4\pi^2 \mu} \langle \vec{\kappa}' | M | \vec{\kappa} \rangle, \tag{7}$$

with $\mu$ the $NN$ reduced mass, and where [24]

$$M = \mathcal{A} + \mathcal{B}(\vec{\sigma}_0 \cdot \hat{n})(\vec{\sigma}_n \cdot \hat{n}) + \mathcal{C}(\vec{\sigma}_0 + \vec{\sigma}_n) \cdot \hat{n}$$
$$+ \mathcal{D}(\vec{\sigma}_0 \cdot \hat{m})(\vec{\sigma}_n \cdot \hat{m}) + \mathcal{E}(\vec{\sigma}_0 \cdot \hat{\ell})(\vec{\sigma}_n \cdot \hat{\ell})$$
$$+ \mathcal{F}[(\vec{\sigma}_0 \cdot \hat{\ell})(\vec{\sigma}_n \cdot \hat{m}) + (\vec{\sigma}_n \cdot \hat{m})(\vec{\sigma}_0 \cdot \hat{\ell})]. \tag{8}$$

Here $\hat{n} = \vec{\kappa} \times \vec{\kappa}' / |\vec{\kappa} \times \vec{\kappa}'|$, $\hat{\ell} = (\vec{\kappa}' + \vec{\kappa}) / |\vec{\kappa}' + \vec{\kappa}|$, and $\hat{m} = \hat{\ell} \times \hat{n}$ are the unit vectors defined by the $NN$ scattering plane.

Of the KMT amplitudes $\mathcal{A}$, $\mathcal{B}$, $\mathcal{C}$, $\mathcal{D}$, $\mathcal{E}$, and $\mathcal{F}$, only $\mathcal{A}$ and $\mathcal{C}$ are used in the context of the present analysis. In calculations these amplitudes are best expressed as complex functions of relative energy $\omega$, momentum transfer $\vec{q} = (\vec{\kappa}' - \vec{\kappa})$, and total $NN$ momentum $\vec{\mathcal{Q}} = (\vec{\kappa}' + \vec{\kappa})/2$ in their c.m. frame. Each amplitude depends on isotopic spin in the form

$$\mathcal{A}(\omega, \vec{\kappa}', \vec{\kappa}) = \mathcal{A}(\omega, \vec{q}, \vec{\mathcal{Q}}) = \mathcal{A}_0 + \mathcal{A}_\tau (\vec{\tau}_0 \cdot \vec{\tau}_n). \qquad (9)$$

### III. STRUCTURE MODELS

#### A. Faddeev calculations for $^{11}$Li

Here $^{11}$Li is considered as a three-body ($^9$Li $+ n + n$) system, the main approximation being to neglect explicit consideration of the internal and spin degrees of freedom of the $^9$Li core. These are treated approximately through the nucleon-core effective interaction. The total wave function is a sum of the three Faddeev components, $\Psi = \Psi_{12} + \Psi_{c1} + \Psi_{c2}$ [8], where 1 and 2 represent the halo neutrons and $c$ the core. Neutron antisymmetrization implies that $\Psi_{c2}$ and $\Psi_{c1}$ are related by permutation of labels, and

$$\Psi = \Psi_{12}(\vec{r}_{12}, \vec{r}_{(12)c}) + (1 + P)\Psi_{c1}(\vec{r}_{c1}, \vec{r}_{(c1)2}). \qquad (10)$$

The total wave function $\Psi$ can be transformed into either set of coordinates, so that

$$\Psi = \bar{\Psi}_{12}(\vec{r}_{12}, \vec{r}_{(12)c}) = \bar{\Psi}_{c1}(\vec{r}_{c1}, \vec{r}_{(c1)2}), \qquad (11)$$

where $\Psi$ and each $\bar{\Psi}$ has unit normalization.

The one-particle density can be written

$$\rho_{11}(\vec{r}) = \hat{\rho}_9(r) + \rho_{\text{halo}}(r), \qquad (12)$$

where $\hat{\rho}_9(r)$ and $\rho_{\text{halo}}(r)$ are the contributions from the core and halo neutrons in the center of mass of the whole nucleus. It follows that the halo density is

$$\rho_{\text{halo}}(\vec{r}) = 2\left(\frac{A}{A-1}\right)^3 \int d\vec{r}_{c1} \left| \bar{\Psi}_{c1}\left(\vec{r}_{c1}, \frac{A}{A-1}\vec{r}\right) \right|^2, \qquad (13)$$

and, assuming that the core internal density is $\rho_9(r)$, then $\hat{\rho}_9(r)$ is obtained by folding with $\rho_c(r)$, the density distribution for the motion of the core center of mass, i.e.,

$$\hat{\rho}_9(\vec{r}) = \int d\vec{r}_c \rho_9(\vec{r} - \vec{r}_c) \rho_c(\vec{r}_c), \qquad (14)$$

where

$$\rho_c(\vec{r}_c) = \left(\frac{A}{2}\right)^3 \int d\vec{r}_{12} \left| \bar{\Psi}_{12}\left(\vec{r}_{12}, \frac{A}{2}\vec{r}_c\right) \right|^2. \qquad (15)$$

In momentum space, in terms of the Fourier transform of each density distribution,

$$\rho_{11}(q) = \hat{\rho}_9(q) + \rho_{\text{halo}}(q), \qquad (16)$$

where

$$\hat{\rho}_9(q) = \rho_9(q) \times \rho_c(q). \qquad (17)$$

In the following we take $^{11}$Li halo density distributions from the Faddeev wave functions of Bang, Thompson, and Zhukov [7,12]. As the detailed structure of this system and the interaction potential between a neutron and the $^9$Li core are not yet known, we consider three proposed Faddeev scenarios, which involve different halo structures and configurations. All models use the realistic supersoft core [SSC(C)] $NN$ potential [25] between the valence neutrons.

(i) The spin-orbit (SO) model [26,7] assumes that the $^{10}$Li ground state is a $0p_{1/2}$ resonance, the $0p_{3/2}$ state being bound with separation energy 4.1 MeV. The $^9$Li core is thus assumed to have a full $0p_{3/2}$ neutron subshell, and the three-body wave function is orthogonalized to the occupied $0s$ and $0p_{3/2}$ states of neutron-core motion. The density used has the $0p_{1/2}$ resonance at $+0.175$ MeV, a $^{11}$Li binding of $-0.32$ MeV, and a matter rms radius of 3.04 fm. The empirical matter radius is $3.10 \pm 0.17$ fm [3].

(ii) The pairing ($P$) model assumes that pairing correlations are dominant, neglects nucleon-core spin-orbit forces, and the valence neutrons are entirely in the relative $^1S_0$ state. The binding energy is $-0.35$ MeV and the matter rms radius is 3.02 fm.

(iii) The $S$-intruder (I1) model has an increased potential strength in the $s$-wave $n + ^9$Li channel, producing a $1s_{1/2}$ scattering length appropriate for a virtual state. The $p$-wave potential gives a $0p_{1/2}$ resonance. In this model ($P3$ of [12]), the three-body wave function is a superposition of $(0p_{1/2})^2$ and $(1s_{1/2})^2$ configurations. A larger rms radius of 3.64 fm is obtained. The model leads to a narrow $^9$Li momentum distribution in the Serber model of $^{11}$Li dissociation, in better agreement with the data [27].

The I1 model thus allows a study of the consequences for $p$-$^{11}$Li elastic scattering observables of structure changes in the $^{11}$Li ground state due to existence of a near-threshold $s$-wave virtual state in $^{10}$Li. To assess the sensitivity of observables to the correct description of the tails of the halo distribution we also present calculations where the $^{11}$Li density is the sum of a Gaussian for the $^9$Li core and a valence density appropriate to oscillator $p_{1/2}$ states,

$$\rho_{\text{halo}}(q) = 2(1 - b_h^2 q^2/6)\exp(-b_h^2 q^2/4). \qquad (18)$$

The range $b_h = 3.58$ fm is chosen to reproduce the rms radius of $^{11}$Li.

#### B. $^9$Li structure models

In the calculations of [7,12] the $^9$Li core is assumed to have a Gaussian density distribution for the purposes of calculating the $^{11}$Li single-particle density. In describing the $^9$Li ground state we consider two simplified structure models. In model I, as in [7,12], we take a Gaussian distribution with a range chosen to reproduce the rms radius $\langle r^2 \rangle_9^{1/2} = 2.32$ fm, i.e.,

$$\rho_9^I(q) = 9\exp(-b_g^2 q^2/4), \quad b_g = 1.89 \text{ fm}. \qquad (19)$$

To assess the sensitivity of elastic scattering to the description of the core we also consider a model II where we follow closely the method applied by Zhukov *et al.* [28] to $^8$He. Here we assume a cluster model for $^9$Li consisting of an $\alpha$-particle-like core, four neutrons in the $p_{3/2}$ shell coupled to spin zero, and a proton in the $p_{3/2}$ shell. We take a Gaussian distribution for the nucleons in the alpha core. The valence nucleons are assumed described within the harmonic oscillator single particle model. In momentum space these densities are, for the alpha core,

$$\rho_\alpha(q) = 4\exp(-b_\alpha^2 q^2/4) \tag{20}$$

and, for the valence neutrons,

$$\rho_n(q) = 4(1 - b_n^2 q^2/6)\exp(-b_n^2 q^2/4). \tag{21}$$

We assume that the proton and neutron $p_{3/2}$ states have the same oscillator range parameter, and so for the proton $\rho_{p_{3/2}}(q) = \rho_n(q)/4$. The range parameters are again chosen to reproduce the rms radius of $^9$Li, i.e.,

$$3b_\alpha^2 + 25b_n^2/4 = 9\langle r^2\rangle_9/2. \tag{22}$$

If we take the same range for the alpha core as was used in $^8$He [28], then $b_\alpha = 1.38$ fm and $b_n = 1.72$ fm. We refer to this as parameter set (a). Other possible pairs of values, consistent with the $^9$Li rms radius, are (b) $b_\alpha = 1.50$ fm, $b_n = 1.67$ fm and (c) $b_\alpha = 1.0$ fm, $b_n = 1.843$ fm. We use the latter parameters as extreme deviations from the more physical set (a) in assessing the sensitivity of observables to the assumed $^9$Li structure. The single-particle density of $^9$Li within model II is

$$\rho_9^{II}(q) = \rho_\alpha(q) + \rho_n(q) + \rho_{p_{3/2}}(q). \tag{23}$$

Taking account of the motion of the $^9$Li core within $^{11}$Li, then, from Eq. (17),

$$\hat\rho_9^{II}(q) = \rho_9^{II}(q)\rho_c(q) = \hat\rho_\alpha(q) + \hat\rho_n(q) + \hat\rho_{p_{3/2}}(q). \tag{24}$$

## IV. OPTICAL POTENTIAL

Given the $^{9,11}$Li structures discussed above, and following Eq. (9), the proton-$^{11}$Li optical potential is written

$$\langle\vec{k}'|U|\vec{k}\rangle = \frac{A-1}{A}[\hat\rho_\alpha(q)\bar{t}_{01}(\omega,q,Q/2,\phi)$$

$$+ \hat\rho_n(q)\bar{t}_{pn}(\omega,q,Q/2,\phi)$$

$$+ \hat\rho_{p_{3/2}}(q)\bar{t}_{pp}(\omega,q,Q/2,\phi)$$

$$+ \rho_{\text{halo}}(q)\bar{t}_{pn}(\omega,q,Q/2,\phi)], \tag{25}$$

where $\phi$ is the angle between the vectors $\vec{Q}$ and $\vec{q}$. Here $\bar{t}_{01}$ is the spin-isospin-averaged $NN$ amplitude, for the closed shell alpha core, and $\bar{t}_{pn}$ is the spin-averaged $pn$ amplitude, due to assumed closed $p_{3/2}$ and $p_{1/2}$ (halo) neutron subshells. At present we do not treat fully the spin dependence associated with the incident proton-bound $p_{3/2}$ proton interaction. We take the spin average, with respect to the struck particle, of the $pp$ transition amplitude, and so possible spin-

dependent contributions, other than the conventional spin-orbit force, are neglected in taking $\bar{t}_{pp}$. We take account of the finite mass of the $^9$Li core in Eq. (25) by the use of the convoluted densities $\hat\rho$ of Eq. (24). The same procedure was carried out implicitly in the treatment of the $p$-$^8$He system at 72 MeV [10] where the range parameter of the alpha core is not that of a free $\alpha$ particle but includes recoil effects [28].

The central and spin-orbit components of the optical potential are therefore

$$\langle\vec{k}'|U|\vec{k}\rangle = U_c(\vec{k}',\vec{k}) + U_{\ell s}(\vec{k}',\vec{k})\vec\sigma_0\cdot\hat{n}, \tag{26}$$

with $\hat{n}$ the unit normal to the $NA$ scattering plane. With the normalizations adopted in Eqs. (20) and (21) for the core and $p_{3/2}$ nucleon densities, the potential form factors are

$$U_c(\vec{k}',\vec{k}) = \frac{A-1}{A}\left[-\frac{\hbar^2}{4\pi^2\mu}\right][\mathcal{A}_0\hat\rho_\alpha(q) + \mathcal{A}_{pn}\hat\rho_n(q)$$

$$+ \mathcal{A}_{pp}\hat\rho_{p_{3/2}}(q) + \mathcal{A}_{pn}\rho_{\text{halo}}(q)], \tag{27}$$

$$U_{\ell s}(\vec{k}',\vec{k}) = \frac{A-1}{A}\left[-\frac{\hbar^2}{4\pi^2\mu}\right][\mathcal{C}_0\hat\rho_\alpha(q) + \mathcal{C}_{pn}\hat\rho_n(q)$$

$$+ \mathcal{C}_{pp}\hat\rho_{p_{3/2}}(q) + \mathcal{C}_{pn}\rho_{\text{halo}}(q)], \tag{28}$$

with $\mathcal{A}_0 \equiv \mathcal{A}_0(\omega,q,Q/2,\phi)$, etc., given by Eq. (9). Studies of the $NN$ amplitude have shown that, for the central and spin-orbit amplitudes $\mathcal{A}$ and $\mathcal{C}$, the variation with angle $\phi$ is very slow [21,29]. Thus we take the on-shell value $\phi = \pi/2$ in the evaluation of these amplitudes. The proton-neutron and proton-proton amplitudes $\mathcal{A}_{pn}$ and $\mathcal{A}_{pp}$ are

$$\mathcal{A}_{pn} = \mathcal{A}_0 - \mathcal{A}_\tau, \quad \mathcal{A}_{pp} = \mathcal{A}_0 + \mathcal{A}_\tau, \tag{29}$$

and similarly for $\mathcal{C}_{pn}$ and $\mathcal{C}_{pp}$.

These momentum space forms give a particularly clear view of the dependence of the optical potential upon the different components of the target density. They show also how effects due to these components having very different spatial ranges, and hence different momentum space distributions, cannot simply be untangled from the intrinsic momentum space behavior of the $NN$ interaction. The importance of each component of the density to the central and spin-orbit terms of the optical potential is driven by the extent to which these momentum space behaviors overlap, and will be different for the core and halo and spin and spin-independent components. We return to these considerations when discussing the results of the calculations of reaction observables. It should be noted that the calculated optical potential is nonlocal and requires knowledge of the $NN$ amplitudes both on and off the energy shell.

For the evaluation of the appropriate $NN$ energy parameter $\omega = E_0 - \hbar^2 Q^2/4m$ we make the usual assumptions that the momentum of the projectile is fixed at the on-shell value $k_0$ and that the dominant momenta of the struck nucleon are small. These should be particularly appropriate for the longer ranged contributions to the optical potential arising from the valence (halo) nucleons, where the nucleons interact in regions of low matter density and are of lower momenta. In this limit the $NN$ energy is assumed fixed with $\omega = E_0/2$
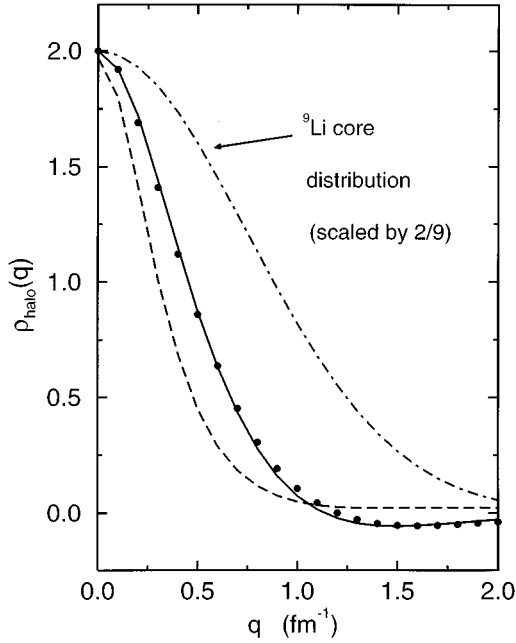
FIG. 1. $^{11}$Li halo neutron density distributions in momentum space, for the pairing ($P$, solid line), spin-orbit (SO, solid points), and intruder I1 (long dashed) Faddeev wave functions. The dot-dashed line shows the Gaussian density description for the $^9$Li core scaled to 2 at $q=0$.

[20], the impulse approximation. This is the value used in the calculation of the $NN$ amplitude.

For $^{11}$Li the $\hat{\rho}$ entering Eqs. (25), (27), and (28) are those of Eq. (24), where $\rho_\alpha$, $\rho_n$, and $\rho_{p_{3/2}}$ are given by Eqs. (20) and (21) for core model II. For core model I we replace $\rho_\alpha = \rho_n = 4\rho_{p_{3/2}}$ where $\rho_\alpha = 4\rho_9^I/9$ of Eq. (19). In the $^9$Li case then $\rho_{\text{halo}} = 0$ and we replace $\hat{\rho}_\alpha = \rho_\alpha$, etc., in Eqs. (27) and (28).

## V. RESULTS

In all calculations the $NN$ scattering amplitudes are calculated exactly, both on and off the energy shell, from the Paris [29,30] $NN$ potential model. What is actually required are the central and spin-orbit Wolfenstein amplitudes $\mathcal{A}$ and $\mathcal{C}$.

### A. Structure models

We use three theoretical scenarios for the halo structure of $^{11}$Li. Figure 1 presents the two neutron halo densities $\rho_{\text{halo}}$, in momentum space, for the pairing ($P$, solid line), spin-orbit (SO, solid points), and intruder I1 (long dashed) Faddeev wave functions described in Sec. III A. All reproduce the empirical binding energy of $^{11}$Li and have appropriate three-body asymptotics. For comparison the dot-dashed line shows the extent of the single Gaussian density description $\rho_9^I$ for the $^9$Li core, which has been scaled to 2 at $q=0$, to aid comparison with the halo distributions.

In configuration space, the $P$ and SO models possess very similar density distributions in the extreme tail of the halo density but can differ substantially in the region of overlap with the $^9$Li core. In momentum space, as in configuration
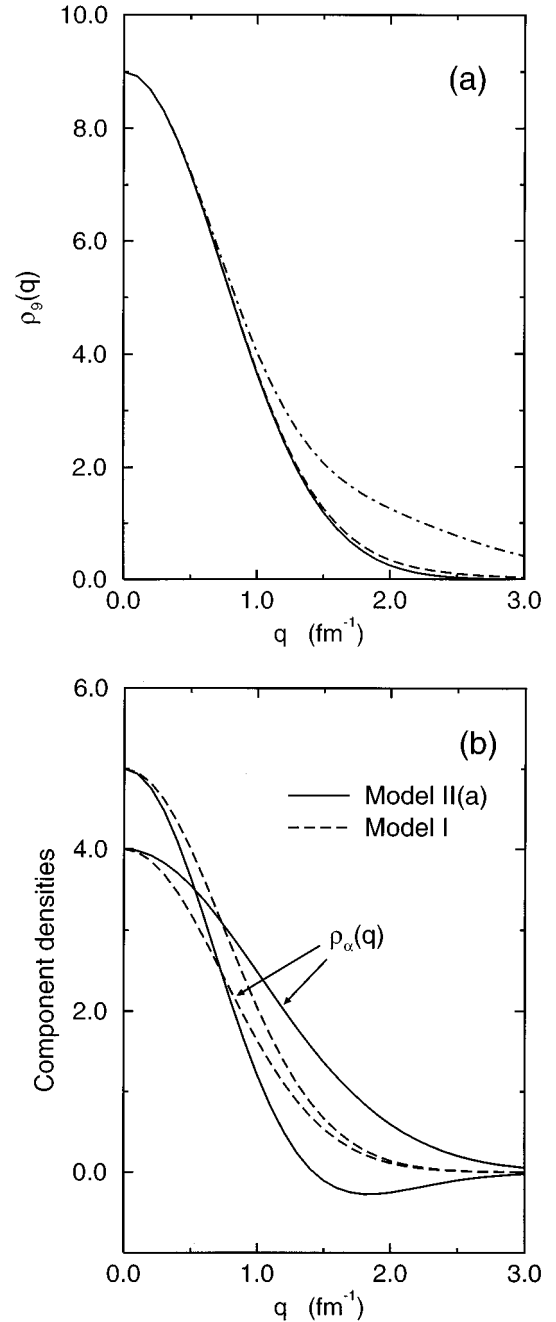


FIG. 2. (a) $^9$Li densities in momentum space for the Gaussian model $\rho_9^I$ (solid line) and the oscillator model $\rho_9^{II}$, using parameter sets (a) (dashed line) and (c) (dash-dotted line). Part (b) shows the $\rho_\alpha$ and $\rho_n + \rho_{p_{3/2}}$ contributions separately for the $\rho_9^I$ (dashed curves) and $\rho_9^{II}$, set (a), (solid curves) models.

space, the SO and $P$ models lead to rather similar distributions. The sensitivity of proton elastic scattering to these different models is discussed quantitatively in the following. The I1 intruder model generates a particularly different density and is expected to generate more extreme differences upon observables.

Figure 2(a) shows the $^9$Li core densities evaluated assuming the single Gaussian $\rho_9^I$ (solid line) model of Eq. (23) and also the oscillator model $\rho_9^{II}$, using parameter sets (a) (dashed line) and (c) (dash-dotted line) of Eq. (19). All mod-
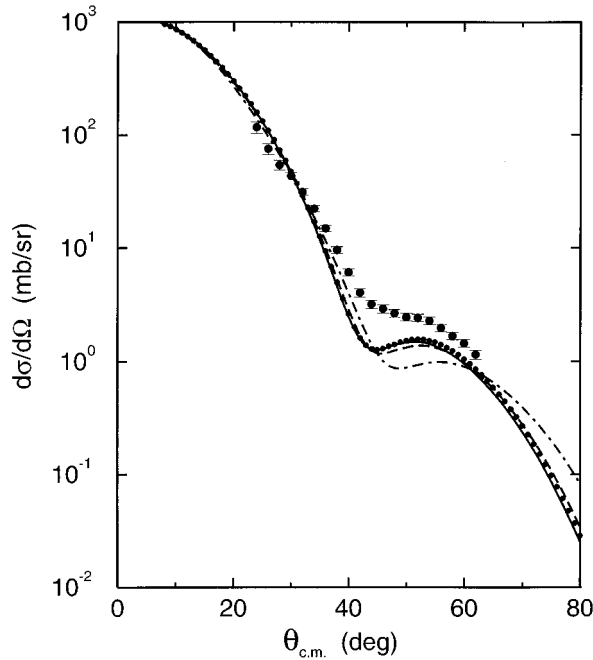
FIG. 3. Experimental and calculated differential cross section angular distributions for $p$-$^{11}$Li scattering at 62 MeV/nucleon. The calculations use the pairing ($P$, solid line), spin-orbit (SO, solid points), and intruder I1 (long dashed line) descriptions for the halo distribution. The dot-dashed line results when using the oscillator model for the valence nucleon distribution. Model I is assumed for the $^9$Li core.

FIG. 4. Calculated and experimental differential cross section angular distributions for $p$-$^9$Li scattering at 60 MeV/nucleon. The curves are the results using the Gaussian $\rho_9^{\mathrm{I}}$ (dashed) and oscillator model, $\rho_9^{\mathrm{II}}$ (a) (solid line) and (c) (dash-dotted line), densities.

els reproduce the empirical $^9$Li matter rms radius. The results for parameter set (b) are quite similar to those for set (a) and, for clarity, are not shown on the figure. The apparent similarity of these densities, from for instance the $\rho_9^{\mathrm{I}}$ (solid) and $\rho_9^{\mathrm{II}}$, set (a), (dashed) models, is somewhat misleading. While the total one-body densities are indeed similar, they result from quite different spin-isospin density decompositions of the nine nucleons. For model II, the density is the sum of $\rho_\alpha$, $\rho_n$, and $\rho_{p_{3/2}}$ terms given by Eqs. (20) and (21), with quite different range parameters. For model I, however, $\rho_\alpha = \rho_n = 4\rho_{p_{3/2}}$, where $\rho_\alpha = 4\rho_9^{\mathrm{I}}/9$, all components having the same range. This distinction is important in the context of Eqs. (27) and (28) where each term multiplies a particular spin or isospin average of the $NN$ amplitude. The constituent contributions $\rho_\alpha$ and $\rho_n + \rho_{p_{3/2}}$ are shown separately in Fig. 2(b) for the $\rho_9^{\mathrm{I}}$ (dashed curves) and $\rho_9^{\mathrm{II}}$, set (a), (solid curves) models. The longer range in momentum space of the more realistic treatment of the alpha core component in model II is evident.

## B. Elastic scattering observables

We proceed to study the effects of the different models of the halo and core distributions upon elastic scattering observables for the $p$-$^{11}$Li system. Figure 3 shows the experimental [13] differential cross section angular distribution for $p$-$^{11}$Li scattering at 62 MeV/nucleon and those calculated using the theoretical density distributions. The calculations are fully off-shell optical potential calculations resulting from the evaluation of Eqs. (27) and (28) without further approxi-
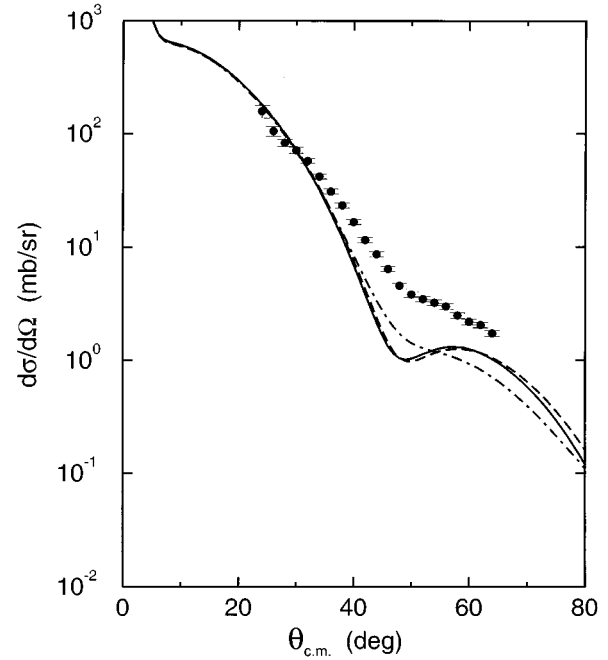
mation. The figure shows the calculated cross sections using the pairing ($P$, solid line), spin-orbit (SO, solid points), and intruder I1 (long dashed line) descriptions for the halo distribution. Here model I is assumed for the $^9$Li core. While the calculated cross section angular distributions show some sensitivity to the different Faddeev models, it is apparent that, unlike the earlier theoretical agreement with the $p$-$^8$He data at 72 MeV [10], the $p$-$^{11}$Li data are not reproduced by any model. In particular the angular dependence of the data at forward angles is not described, the calculations falling too rapidly with scattering angle in the angular range $20°$–$40°$. There are only small differences between observables for these structure models. The importance of a correct description of the halo tail is shown by the dash-dotted line which results when using the oscillator model description of the valence nucleon distribution. The result makes clear the sensitivity to the correct description of the tail of the halo density distribution of the Faddeev models.

We note that the first order KMT optical potential discussed here will include contributions in which the incident and struck nucleons are in the continuum [21,31]. These are assumed to scatter as free particles. Thus elements of the $^{11}$Li breakup continuum will be already included within the calculated single scattering KMT interaction. It would be extremely interesting to investigate further the relationship between these calculations and breakup contributions calculated using few-body descriptions [17]. The latter show the breakup effects are significant on the calculated cross section and result in a more rapid decrease in the cross section angular distribution with angle.

Figure 4 shows the calculated and experimental [13] differential cross section angular distributions for $p$-$^9$Li scattering at 60 MeV/nucleon. The curves are the results calculated
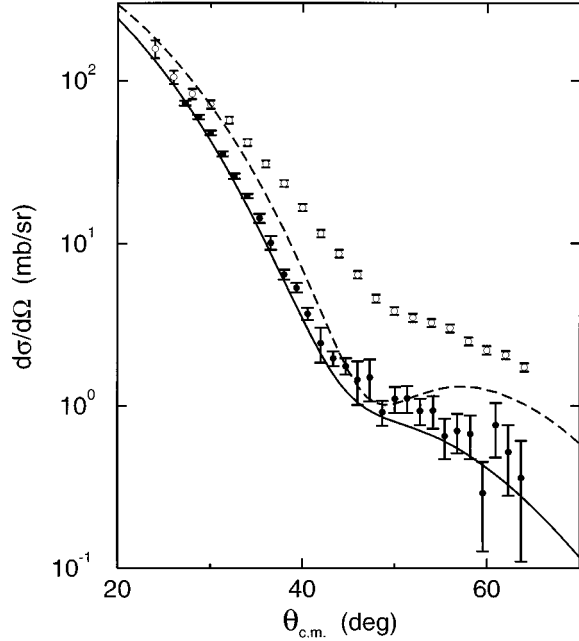
FIG. 5. Experimental data for the $p$-$^8$He system at 72 MeV (solid circles) and the $p$-$^9$Li system at 60 MeV (open circles). The curves show the calculated angular distributions for proton scattering from $^8$He at 72 MeV (solid curve) and from $^9$Li at 60 MeV using $\rho_9^{II}$ set (a) (dashed curve).

using the single Gaussian $\rho_9^I$ (dashed) and oscillator model, $\rho_9^{II}$ (a) (solid) and (c) (dash-dotted), densities. The $p$-$^9$Li experimental data, like the $^{11}$Li data, are not reproduced. We note the similar failure to reproduce the slope of the observed distribution at forward angles and the relative insensitivity of the calculations in that angular region to the different models used. Here, all $^9$Li densities used have been constrained to reproduce the empirical $^9$Li rms matter radius. The model II forms have also been motivated by the success of the cluster orbital shell model approximation (COSMA) (oscillator) model for the $p$-$^8$He system [10]. Calculations by Bertulani and Sagawa [32] use more sophisticated $^9$Li descriptions, based on Hartree-Fock calculations [6]. The cross sections, calculated using Glauber theory, show very similar qualitative features to those of the present work. To date, only phenomenological potential fits [13,17] have been able to produce a satisfactory description of these experimental data. It is clear, in the context of $p$-$^{11}$Li calculations based on few-body descriptions of the halo nucleus, described above, that the agreement of the microscopic multiple scattering calculations with the available data is already unsatisfactory at the level of the nucleon-$^9$Li core subsystem.

The failure of the microscopic calculations for the mass 9 core is amplified by reference to Fig. 5, which shows the data (solid points) [14] and results of microscopic calculations for the $p$-$^8$He system (solid curve) [10] at 72 MeV/nucleon. The rms matter radius of $^8$He in these calculations is 2.52 fm [3], to be compared with the values 2.32 fm for $^9$Li, and values from 3.02 to 3.64 fm for the three-body models used for $^{11}$Li. The calculated and experimental $p$-$^9$Li angular distributions at 60 MeV are shown by the open points and dashed curve, respectively. The $^8$He density is that of Ref. [10] and
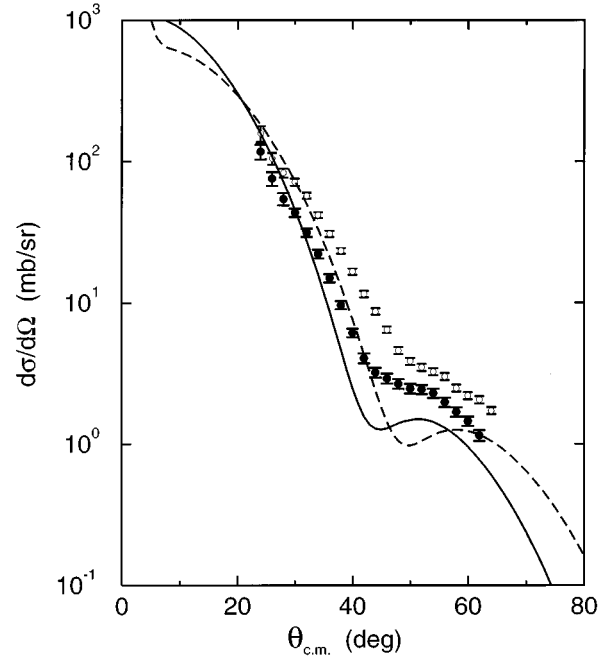


FIG. 6. Experimental elastic cross section angular distributions for $p$-$^{11}$Li at 62 MeV/nucleon (solid circles) and $p$-$^9$Li at 60 MeV/nucleon (open circles). The cross sections calculated assuming the pairing model Faddeev wave function for $^{11}$Li and the model I core density for $^9$Li are shown by the solid and dashed curves, respectively.

the $^9$Li density is the (a) version of model $\rho_9^{II}$, with the same alpha core radius parameter as for $^8$He.

The calculated $^8$He and $^9$Li angular distributions are similar. On the other hand, the experimental data show a very different behavior with momentum transfer and would indicate a major structural difference between the $^9$Li and $^8$He systems. Close inspection shows that the first three small angle data points for $^9$Li follow the trend of the microscopic calculations but the experimental data then change slope markedly at 30°, a feature absent from the calculations.

Figure 6 compares the measured angular distributions for $^{11}$Li at 62 MeV (solid circles) and $^9$Li at 60 MeV (open circles) [13]. The cross sections calculated assuming the pairing model Faddeev wave function for $^{11}$Li and the model I core density for $^9$Li are also shown by the solid and dashed curves, respectively. Both the fall of the cross sections with angle and their diffractive structure are too strong in the calculations. The differences between the calculations and between the two sets of experimental data suggest, however, that an improved description of the $^9$Li core interaction would lead also to an improved description of the $^{11}$Li data, as is obtained when phenomenological descriptions of the core interaction are used [17].

## C. Core and valence particle contributions

We consider additional calculations to assess the importance of the core and valence nucleon contributions to the central and spin-orbit components of the potentials. Our model allows the core and valence particle $NN$ amplitudes, that is, the $\mathcal{C}$ and $\mathcal{A}$ in Eqs. (27) and (28), to be selectively
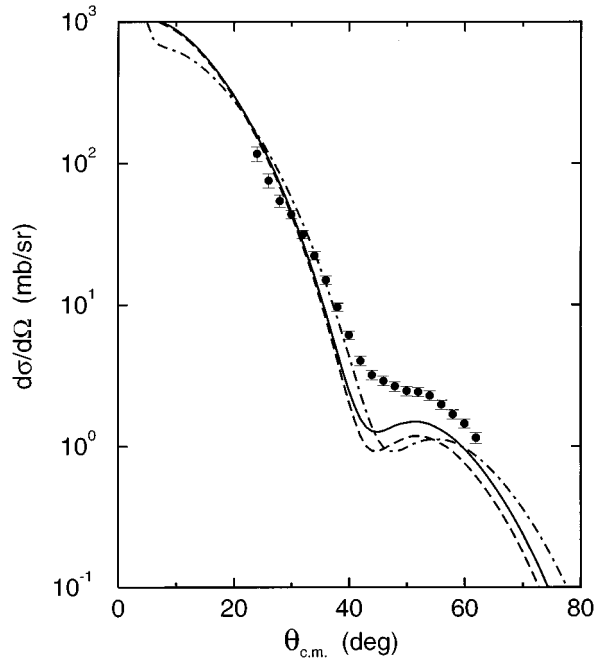
FIG. 7. Calculated differential cross section angular distributions for $p$-$^{11}$Li scattering at 62 MeV. The solid curve is the full pairing model calculation. The dot-dashed curve is obtained when the halo particles are assumed to be noninteracting. The dashed curve is the calculation in the complete absence of the spin-orbit terms in the $p$-$^{11}$Li interaction, i.e., $\mathcal{C}_0=\mathcal{C}_{pn}=\mathcal{C}_{pp}=0$.
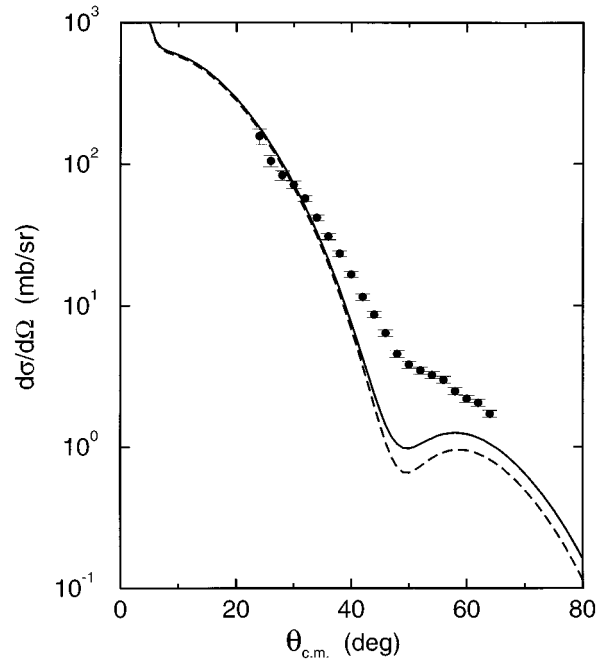


FIG. 8. Calculated differential cross section angular distributions for $p$-$^9$Li scattering at 60 MeV/nucleon. The solid curve is the result using the Gaussian density $\rho_9^{\mathrm{I}}$. The dashed line shows the calculation in the complete absence of the spin-orbit terms in the $p$-$^9$Li interaction, i.e., that $\mathcal{C}_0=\mathcal{C}_{pn}=\mathcal{C}_{pp}=0$.

switched on or off while retaining the correct proton-target kinematics. Figures 7 and 8 show such calculations for $^{11}$Li and $^9$Li, respectively. It was shown [10] that for $^8$He, the valence nucleon contribution to the central distortion was large but had little effect on the spin-orbit interaction. The significant spin dependence seen there arose from the alpha-like core. We show this spin transparency of the extended valence particles to be a general feature. That is, cross section angular distributions are sensitive to the spin-dependent interaction but this part of the interaction carries little information on the valence particle distribution.

Figure 7 shows the calculated angular distributions for $^{11}$Li at 62 MeV. The solid curve is the full pairing model calculation using $\rho_9^{\mathrm{I}}(q)$ for the core density. The dot-dashed curve shows the cross section were the halo nucleons noninteracting, i.e., when we set $\mathcal{A}_{pn}=\mathcal{C}_{pn}=0$ multiplying $\rho_{\mathrm{halo}}$ in Eqs. (27) and (28). The changes induced show that the halo has a significant effect on the optical potential. This effect is, however, due only to the central part of the interaction and, when only $\mathcal{C}_{pn}$ multiplying $\rho_{\mathrm{halo}}$ is set to zero, i.e., when the spin-orbit interaction due to the halo particles is removed, the calculation essentially coincides with the full calculation and is not shown. The dashed line shows the calculation in the complete absence of spin-orbit terms, that is, replacing $\mathcal{C}_0=\mathcal{C}_{pn}=\mathcal{C}_{pp}=0$ in Eq. (28). The spin-orbit interaction effects are seen to be quite considerable, given the quoted accuracy of the experimental data.

Figure 8 shows corresponding calculations for $^9$Li at 60 MeV. The solid curve is the full calculation using the Gaussian density $\rho_9^{\mathrm{I}}(q)$. The dashed line shows the calculation in the limit that $\mathcal{C}_0=\mathcal{C}_{pn}=\mathcal{C}_{pp}=0$. The spin-orbit force effects

are again very significant. When using the $\rho_9^{\mathrm{II}}(q)$ (a) density, as was observed for $^8$He, the bulk of the spin dependence is attributable to the alpha core component in the $^9$Li. That the calculated spin dependence for $^9$Li is slightly larger than that for $^{11}$Li is the result of the use of the convoluted $\hat{\rho}_9(q)$ rather than $\rho_9(q)$.

These observed sensitivities of the cross section angular distributions to the valence particle central distortions and the core nucleon spin-orbit distortions are now discussed. They are best understood by reference to the ranges of the core and valence particle momentum space densities and the momentum transfer dependence of the free $NN$ amplitudes $\mathcal{C}$ and $\mathcal{A}$. The calculation of the optical potentials involves the $NN$ amplitudes both on and off the energy shell; however, the forms of the amplitudes on-shell are instructive here. The on-shell $\mathcal{A}$ and $\mathcal{C}$ of the Paris interaction, for the nucleon-nucleus system at 72 MeV, are presented in Figs. 9 and 10. Figure 9 shows the real (solid curves) and imaginary (dashed curves) parts of the central amplitudes $\mathcal{A}_0$, $\mathcal{A}_{pn}$, and $\mathcal{A}_{pp}$ as a function of momentum transfer. Figure 10 shows the corresponding spin-orbit terms $\mathcal{C}_0$, $\mathcal{C}_{pn}$, and $\mathcal{C}_{pp}$.

The contribution from each involves its product with the appropriate target density component, shown in Figs. 1 and 2. The peaking of the $\mathcal{A}$ at $q=0$ means that all density components will contribute to the real and imaginary parts of the central potential but with different magnitudes. The incident proton interaction with the halo density in $^{11}$Li is via the stronger $\mathcal{A}_{pn}$ amplitude, as is the four $p_{3/2}$ neutrons, comprising $\hat{\rho}_n(q)$, in $^{11}$Li, $^9$Li, and $^8$He. The result is a strong dependence of the central component of the optical potential on the valence nucleon components. Also apparent is that calculations which make a zero range ($\mathcal{A}=\mathrm{const}$) approxi-
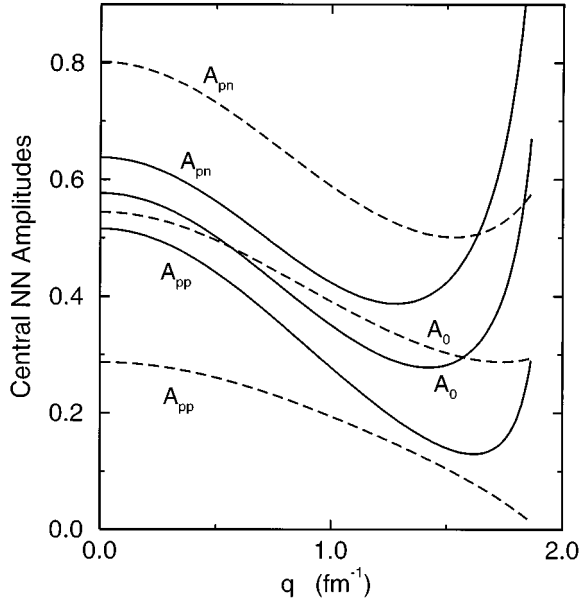
FIG. 9. Real (solid curves) and imaginary (dashed curves) parts of the on-shell central Paris $NN$ amplitudes $\mathcal{A}_0$, $\mathcal{A}_{pn}$, and $\mathcal{A}_{pp}$ as a function of momentum transfer for nucleon-nucleus scattering at 72 MeV.

mation for the $NN$ amplitudes will not correctly account for the relative importance of the different density components. In particular, the longer ranged momentum space terms, such as the alpha contribution of the $^9$Li core in model II and the $^9$Li core itself in model I, are likely to be overestimated relative to those of the valence nucleons.

Inspection of the $\mathcal{C}$, with their maxima at $1–1.2$ fm$^{-1}$, suggests that the spin-orbit potential contribution from the localized momentum space valence particle densities will be
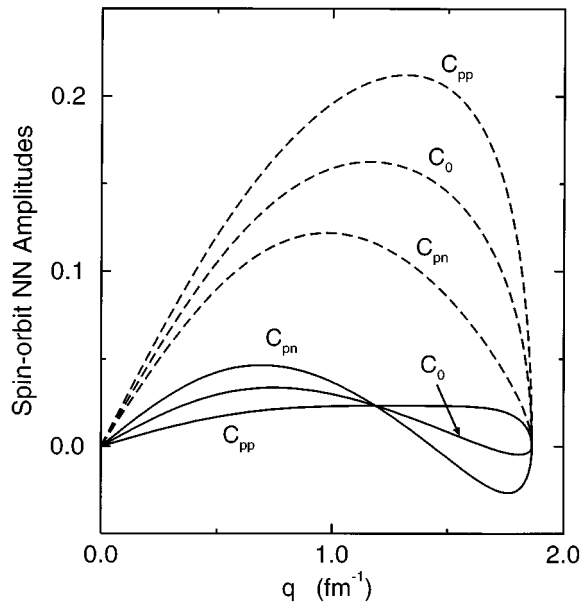


FIG. 10. Real (solid curves) and imaginary (dashed curves) parts of the on-shell spin-orbit Paris $NN$ amplitudes $\mathcal{C}_0$, $\mathcal{C}_{pn}$, and $\mathcal{C}_{pp}$ as a function of momentum transfer for nucleon-nucleus scattering at 72 MeV.

small. The more spatially localized core components, however, with their correspondingly wider momentum space distributions, Fig. 1, lead to significant overlap with the $\mathcal{C}$ amplitudes. Further, the $\mathcal{C}_{pn}$ term, relevant to the interaction with the halo density in $^{11}$Li and the four $p_{3/2}$ neutrons in $^9$Li and $^8$He, is itself weaker than the $\mathcal{C}_{pp}$ and spin-isospin-averaged $\mathcal{C}_0$ amplitudes. When using models $\rho_9^{II}(q)$ the $\mathcal{C}_0$ amplitude acts on the alpha core component, Fig. 2(b), with significant strength. This clarifies the observation above for $^9$Li, and of Ref. [10] for $^8$He, that in such models the spin-orbit interaction arises almost exclusively from this core contribution.

Finally, since the density of the $^9$Li core within $^{11}$Li is somewhat more extended, due to its convolution with the core c.m. motion, $\hat{\rho}_9(q)$ is of shorter range in momentum space than $\rho_9(q)$ with consequent reduced spin dependence in the $^{11}$Li system, as observed earlier.

The remarks above are expected to be quite general. They demonstrate that while calculated cross section angular distributions are sensitive to assumed valence nucleon structures, and to the spin dependence of the proton target interaction, these sensitivities result from quite different parts of the target structure. The momentum space form of the central $NN$ amplitudes results in strong corrections to the central parts of the optical potential due to the skin or halo of valence particles, particularly neutrons. The finite range of the $NN$ force is vital to including the balance between these different contributions correctly. On the other hand, the spin-orbit $NN$ amplitudes do not overlap strongly with the short range momentum space forms associated with a neutron halo or skin and these valence particles do not contribute effectively to the spin-orbit component of the optical potential. The core spin-orbit contributions, however, have considerable effects on the calculated angular distributions; moreover, the detailed structure of the core itself is also involved.

## VI. CONCLUSIONS

The microscopic optical potential for proton elastic scattering from $^9$Li and $^{11}$Li targets is evaluated using the single scattering approximation to the KMT multiple scattering expansion of the optical potential. This includes fully the finite range of the $NN$ amplitude and the central and spin-orbit components of the optical potential arising from the free $NN$ transition amplitude.

Calculations are compared with the available data at energies near 60 MeV/nucleon and with calculations and data for the $^8$He system at similar energy. The $p$-$^9$Li and $^{11}$Li experimental data are not reproduced, the slope of the calculated angular distributions being too steep at forward angles. There are large differences between the experimental angular distributions for $^9$Li and $^8$He, but not between the calculations, suggesting a major structural difference between the $^9$Li and $^8$He systems. The calculations suggest that the $^9$Li core structure is not realistically described by simple, oscillator-inspired, structure models which are successful for $^8$He.

The $^{11}$Li cross section is found to be insensitive to that part of the spin-orbit force due to the halo nucleons but strongly affected by the central distortion due to these particles. These observed sensitivities were discussed in terms

of the ranges of the core and valence particle momentum space densities and the momentum transfer dependence of the free $NN$ amplitudes. The results of such an analysis are very general. While the momentum space form of the central $NN$ amplitudes will overlap strongly with the skin or halo particle densities, the $NN$ spin-orbit amplitudes will not overlap these momentum components effectively. The core spin-orbit contributions, however, have considerable effects on the calculated angular distributions. The finite range of the $NN$ force is crucial in describing these contributions correctly.

[1] *Proceedings of the First International Conference on Radioactive Nuclear Beams*, Berkeley, CA, edited by W.D. Meyers, J.M. Nitschke, and E.B. Noeman (World Scientific, Singapore, 1990).

[2] I. Tanihata *et al.*, Phys. Lett. **160B**, 380 (1985); I. Tanihata, H. Hamaguchi, O. Hashimoto, Y. Shida, N. Yoshikava, K. Sugimoto, O. Yamakawa, T. Kobayashi, and N. Takahashi, Phys. Rev. Lett. **55**, 2676 (1985).

[3] I. Tanihata, T. Kobayashi, O. Yamakawa, S. Shimoura, K. Ekuni, K. Sugimoto, N. Takahashi, T. Shimoda, and H. Sato, Phys. Lett. B **206**, 592 (1988).

[4] M. Fukuda *et al.*, Phys. Lett. B **268**, 339 (1991); A.C. Villari *et al.*, *ibid.* **268**, 345 (1991).

[5] I. Tanihata, Nucl. Phys. **A522**, 275c (1990).

[6] G. Bertsch, B.A. Brown, and H. Sagawa, Phys. Rev. C **39**, 1154 (1991).

[7] J.M. Bang and I.J. Thompson, Phys. Lett. B **270**, 201 (1992).

[8] M.V. Zhukov, D.V. Fedorov, B.V. Danilin, J.S. Vaagen, J.M. Bang, and I.J. Thompson, Nucl. Phys. **A552**, 353 (1993).

[9] M.V. Zhukov, B.V. Danilin, D.V. Fedorov, J.M. Bang, I.J. Thompson, and J.S. Vaagen, Phys. Rep. **231**, 151 (1993).

[10] R. Crespo, J.A. Tostevin, and R.C. Johnson, Phys. Rev. C **51**, 3283 (1995).

[11] R. Kryger *et al.*, Phys. Rev. C **47**, R2439 (1993); B.M. Young *et al.*, *ibid.* **49**, 279 (1994).

[12] I.J. Thompson and M.V. Zhukov, Phys. Rev. C **49**, 1904 (1994).

[13] C.B. Moon, M. Fujimaki, S. Hirenzaki, N. Inabe, K. Katori, J.C. Kim, T. Kobayashi, T. Kubo, H. Kumagai, S. Shimoura, T. Suzuki, and I. Tanihata, Phys. Lett. B **297**, 39 (1992).

[14] A.A. Korsheninnikov *et al.*, Phys. Lett. B **316**, 38 (1993).

[15] L.V. Chulkov, C.A. Bertulani, and A.A. Korsheninnikov, Nucl. Phys. **A587**, 291 (1995).

[16] S. Hirenzaki, H. Toki, and I. Tanihata, Nucl. Phys. **A552**, 57 (1993).

[17] Y. Suzuki, K. Yabana, and Y. Ogawa, Phys. Rev. C **47**, 1317 (1993).

[18] A.K. Kerman, H. McManus, and R.M. Thaler, Ann. Phys. (N.Y.) **8**, 551 (1959).

[19] H.F. Arellano, F.A. Brieva, and W.G. Love, Phys. Rev. C **41**, 2188 (1990); H.F. Arellano, W.G. Love, and F.A. Brieva, *ibid.* **43**, 2734 (1991).

[20] R. Crespo, R.C. Johnson, and J.A. Tostevin, Phys. Rev. C **41**, 2257 (1990).

[21] R. Crespo, R.C. Johnson, and J.A. Tostevin, Phys. Rev. C **44**, R1735 (1991); **46**, 279 (1992).

[22] Ch. Elster, T. Cheon, E.F. Redish, and P.C. Tandy, Phys. Rev. C **41**, 814 (1990); C.R. Chinn, Ch. Elster, and R.M. Thaler, *ibid.* **44**, 1569 (1991).

[23] C.R. Chinn, Ch. Elster, R.M. Thaler, and S.P. Weppner, Phys. Rev. C **51**, 1418 (1995).

[24] L. Wolfenstein and J. Ashkin, Phys. Rev. **85**, 947 (1952).

[25] R. de Tourreil and D.W.L. Sprung, Nucl. Phys. **A242**, 445 (1975).

[26] G.F. Bertsch and H. Esbensen, Ann. Phys. (N.Y.) **209**, 327 (1991).

[27] N.A. Orr *et al.*, Phys. Rev. Lett. **69**, 2050 (1992).

[28] M.V. Zhukov, A.A. Korsheninnikov, and M.H. Smedberg, Phys. Rev. C **50**, R1 (1994).

[29] E.F. Redish and K. Stricker-Bauer, Phys. Rev. C **36**, 513 (1987).

[30] M. Lacombe, B. Loiseau, J.M. Richard, R. Vinh Mau, J. Côté, P. Pires, and R. de Tourreil, Phys. Rev. C **21**, 861 (1980).

[31] P.C. Tandy, E.F. Redish, and D. Bollé, Phys. Rev. Lett. **35**, 921 (1975); Phys. Rev. C **16**, 1924 (1977).

[32] C.A. Bertulani and H. Sagawa, Nucl. Phys. **A588**, 667 (1995).